ELSEVIER

International Journal of Solids and Structures 41 (2004) 2977–2993

INTERNATIONAL JOURNAL OF SOLIDS and STRUCTURES

www.elsevier.com/locate/ijsolstr

A new three-dimensional interface finite element to simulate fracture in composites

Javier Segurado, Javier LLorca *

Department of Materials Science, Polytechnic University of Madrid, ETS de Ingenieros de Caminos, 28040 Madrid, Spain

Received 4 September 2003; received in revised form 10 December 2003

Available online 27 February 2004

Abstract

A new three-dimensional quadratic interface finite element is developed. The element is made up by two 6-noded triangular surfaces which initially lie together and connect the faces of adjacent quadratic tetrahedra, the only elements supported by automatic meshing algorithms. The element is introduced within the framework of implicit analysis and large displacements, and can include any traction–separation law at the interface. It is aimed at simulating damage by particle fracture and interface decohesion in composites by the numerical simulation in three-dimensions of a representative volume element which reproduces the microstructure. The element was validated by comparison with previous results of sphere–matrix decohesion obtained in two-dimensional, axisymmetric conditions. In addition, a new control technique is presented to obtain the whole load–displacement curve at a reasonable computational cost when progressive damage throughout the model (due to the simultaneous development of multiple cracks) leads to severe numerical instabilities. The potential of the new element and the control technique were checked in simulations including sphere fracture in composites made up of random distribution of elastic spheres within an elasto-plastic matrix.

Keywords: Finite elements; Computational micromechanics; Composites; Particle fracture; Interface decohesion

1. Introduction

The processing speed of digital computers and the techniques of parallel computing advance rapidly, and the mechanical behavior of heterogeneous materials can nowadays be analyzed through numerical simulation in three-dimensions of a representative volume element which mimics accurately the actual microstructure. Applications of this new methodology to particle-reinforced composites (PRC) were pioneered by Gusev (1997) and Michel et al. (1999) in the elastic regime, and it was used by Segurado and LLorca (2002) to obtain an "exact" solution (to a few percent) of a classical problem in solid mechanics: the determination of the elastic constants of a composite material made up of a random and homogeneous

* Corresponding author. Tel.: +34-913-365-375; fax: +34-915-437-845.
E-mail address: jllorca@mater.upm.es (J. LLorca).

0020-7683/$ - see front matter © 2004 Elsevier Ltd. All rights reserved.
doi:10.1016/j.ijsolstr.2004.01.007

distribution of monodisperse elastic spheres embedded in an elastic matrix. More recent developments addressed the elastic behavior of misaligned short fiber-reinforced composites (Lusti et al., 2002) and the simulation of the effects of the particle spatial distribution on the overall elasto-plastic properties in sphere-reinforced composites (Segurado et al., 2003).

Further improvements in the modeling of PRC should be aimed at including the effect of damage, which is known to control many critical mechanical properties such as ductility and fracture toughness. Experimental observations on polymer- and metal-matrix composites reinforced with brittle, stiff ceramic particles have demonstrated that damage was always nucleated at the ceramic reinforcements, the main causes of void nucleation being particle fracture and decohesion at the matrix/reinforcement interface (Moloney et al., 1987; Cantwell and Roulin-Moloney, 1989; González and LLorca, 1998; LLorca, 2000). The prevalence of either mechanism depended on a number a factors, which included matrix, reinforcement, and interfacial strength, the loading mode and the spatial reinforcement distribution.

The patterns of interface decohesion and particle fracture are well known from experimental observations in sphere-reinforced composites (Fig. 1). Particle fracture takes place suddenly by the unstable propagation of a crack perpendicular to the tensile loading axis through the equator of the sphere, while interface decohesion is stable: it begins at the poles of the spheres and propagates gradually through the interface as the applied strain increases. The plastic deformation of the matrix around the sphere leads to the formation of a void in between the sphere halves or at the poles, and composite fracture is often dictated by the formation of a crack by the impingement of the voids nucleated at neighbor particles or by the localization of the plastic deformation in the intervoid matrix (Kanetake et al., 1995; Babout et al., 2001). Computational micromechanics models are ideal tools to study the initiation and progress of damage throughout the microstructure. The simulation of matrix failure within the context of three-dimensional numerical simulations of the composite microstructure was addressed in a previous publication (LLorca

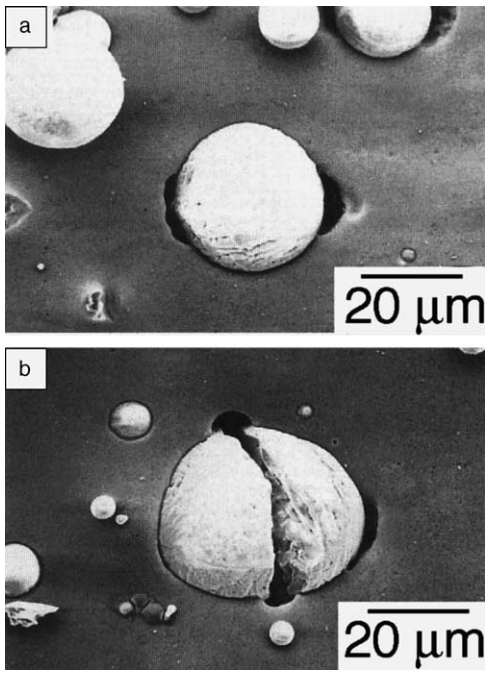

Fig. 1. Damage nucleation in particle-reinforced composites. (a) Interface decohesion. (b) Particle fracture. The composite material was made up of a 6061 Al alloy reinforced with alumina spherical particles. The loading axis was horizontal (Kanetake et al., 1995).

and Segurado, 2004). This paper is focused on the characterization of the nucleation of damage by particle fracture and interface decohesion.

Assuming that the crack path is known *a priori* (either at the sphere/matrix interface or at the equator of the spheres), various strategies can be used to model damage. For instance, Eckschlager et al. (2002) duplicated the nodes at the sphere equator, and linked the degrees of freedom corresponding to the nodes with the same coordinates. Fracture was simulated by releasing all the degrees of freedom across the fracture surface at a constant applied strain when the volume-averaged maximum principal stress in the particle reached a critical value. The extrapolation of this technique to study interface fracture is, however, uncertain, and the physical mechanisms of fracture are better represented by a cohesive crack model. This approach was first introduced by Needleman (1987) to analyze interface decohesion at metal–ceramic interfaces within the framework of computational micromechanics and has been extensively used since to model interface fracture in two-dimensional problems (Tvergaard, 1990; Tvergaard and Hutchinson, 1993; Ghosh et al., 2000). From the discretization viewpoint, the crack is represented by interface elements with zero initial thickness which transmits normal and shear stresses. The magnitude of these stresses depends on the gap in normal and shear displacements between both crack faces, and different constitutive equations can be used to study crack nucleation and propagation through an interface or brittle fracture at the equator of a sphere.

The numerical implementations of the cohesive crack model were mainly carried out in two dimensions and there are few applications in three dimensions. They include the work of Ortiz and Pandolfi (1999) and Pandolfi et al. (2000) within the framework of an explicit integration scheme and of de Andrés et al. (1999), Hashagen and de Borst (2000) and Roychowdhury et al. (2003) for implicit solvers. The cohesive elements used with implicit solvers were always made up by two quadrilateral surfaces connecting brick elements which are normally used to discretize the continuum in three dimensions. However, the discretization of the complex microstructures of PRC has to be done with automatic meshing algorithms which only use tetrahedra, and the use of cohesive crack models to simulate damage requires the corresponding interface elements compatible with the solid tetrahedra.

This paper introduces two new three-dimensional cohesive elements made up of two triangular surfaces which are compatible, respectively, with the standard 10-node tetrahedra solid elements as well as with the *modified* 10-node tetrahedra in Abaqus (2002) and in Thoutireddy et al. (2002). The element is developed using a large displacement formulation, necessary to account for the large voids formed at the interface and within the particles during fracture (Fig. 1). In addition, a new control technique is presented to obtain the whole load–displacement response in a simulation at a reasonable computational cost because the nucleation of damage in the microstructure often leads to numerical instabilities, which delay (or even impede) the convergence. The cohesive elements can use any constitutive equation for the cohesive crack; the one used by Needleman (1987) is implemented to check the new element by comparing the results of the full three-dimensional simulation with the axisymmetric predictions of interface decohesion in a rigid sphere embedded in an elasto-plastic matrix. Once the element had been validated, the control algorithm was checked in simulations including sphere fracture and interface decohesion within the framework of multiparticle cell models.

2. Interface finite element in three-dimensions

2.1. Element formulation

The interface element is made up of two quadratic (6-node) triangular surfaces that connect the faces of two adjacent quadratic tetrahedra. Two versions of the element were developed; the first one, denominated *standard*, is compatible with the standard, isoparametric 10-node tetrahedra. The *modified* interface element

is compatible with the composite tetrahedra of Thoutireddy et al. (2002) and with the modified 10-node tetrahedra of Abaqus (2002). These latter elements have three extra internal degrees of freedom (corresponding to an internal node) and their shape functions are obtained by adding the shape functions of the twelve 4-node linear tetrahedra that compose the modified tetrahedron. This element, developed to alleviate some problems of the standard 10-node tetrahedra for contact problems (particularly in uniform pressure situations), exhibits minimal shear and volumetric locking and is robust during finite deformation.

The two triangular surfaces of the interface element lie together in the initial configuration (zero thickness) and separate as the adjacent solid elements deform (Fig. 2). The relative displacement of the element faces generate normal and shear stresses depending on the constitutive equation of the cohesive crack, which is independent of the element formulation. The interface element has 36 degrees of freedom. The nodal displacements in the global coordinate system are given by the 36×1 column vector $\mathbf{d}_N$ defined as

$$\mathbf{d}_N = \left(d_x^1 \quad d_y^1 \quad d_z^1 \quad d_x^2 \quad d_y^2 \quad d_z^2 \quad \cdots \quad d_x^{12} \quad d_y^{12} \quad d_z^{12} \right)^{\mathrm{T}}, \tag{1}$$

and the relative displacement between paired nodes in the element surfaces is given in global coordinates by the 18×1 column vector $\Delta\mathbf{u}_N$

$$\Delta\mathbf{u}_N = \mathbf{\Phi}^{*}\mathbf{d}_N = \left(\mathbf{I}_{18\times 18} \quad | \quad -\mathbf{I}_{18\times 18} \right)\mathbf{d}_N, \tag{2}$$

where $\mathbf{I}_{n\times n}$ is the identity matrix.

Let $\phi_i(\xi,\eta)$ be the shape function for the node pair i ($i = 1,6$), where ξ and η stand for the natural element coordinates $0 \leqslant \xi \leqslant 1$, $0 \leqslant \eta \leqslant 1$. The relative displacement between the element faces at the point (ξ,η) can be interpolated as a function of relative displacement between paired nodes as

$$\Delta\mathbf{u}(\xi,\eta) = \begin{pmatrix} \Delta u_x(\xi,\eta) \\ \Delta u_y(\xi,\eta) \\ \Delta u_z(\xi,\eta) \end{pmatrix} = \mathbf{\Phi}^{**}(\xi,\eta)\Delta\mathbf{u}_N, \tag{3}$$

where $\mathbf{\Phi}^{**}$ is a 3×18 matrix given by

$$\mathbf{\Phi}^{**}(\xi,\eta) = \left(\phi_1\mathbf{I}_{3\times 3} \quad | \quad \phi_2\mathbf{I}_{3\times 3} \quad | \quad \phi_3\mathbf{I}_{3\times 3} \quad | \quad \phi_4\mathbf{I}_{3\times 3} \quad | \quad \phi_5\mathbf{I}_{3\times 3} \quad | \quad \phi_6\mathbf{I}_{3\times 3} \right). \tag{4}$$

The shape functions ϕ_i ($i = 1,6$) for the standard and modified elements can be found in Appendix A, and Eqs. (2) and (3) lead to

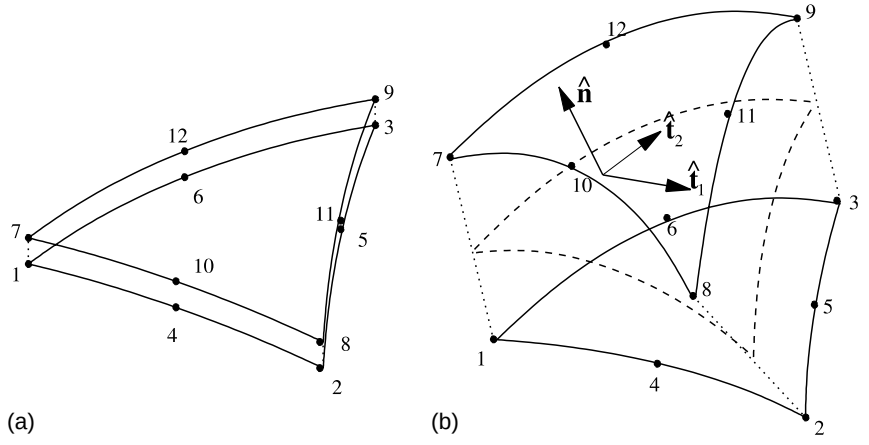

Fig. 2. Interface finite element. (a) Initial configuration with zero thickness. (b) Current configuration showing the reference middle surface.

$$\Delta\mathbf{u}(\xi,\eta) = \mathbf{\Phi}^{**}\mathbf{\Phi}^{*} = \mathbf{\Phi}\mathbf{d}_N, \tag{5}$$

where $\mathbf{\Phi}$ is the 3×36 matrix which computes the relative crack opening at any point of the interface element from the nodal displacements.

Under the large displacement formulation, the local coordinate system of the interface element in the deformed configuration has to be defined to compute the current normal and tangential directions. Ortiz and Pandolfi (1999) used a reference surface given by the middle points between the two (deformed) triangular surfaces (Fig. 2). If the coordinates of the interface element nodes at the initial configuration are given by the 36×1 vector $\mathbf{x}_N$, the reference surface is defined by the coordinates of 6 points in the 18×1 vector $\mathbf{x}_N^R$ computed by linear interpolation of the coordinates of paired nodes in both surfaces in the deformed configuration as

$$\mathbf{x}_N^R = \tfrac{1}{2}(\,\mathbf{I}_{18\times 18} \quad | \quad \mathbf{I}_{18\times 18}\,)(\mathbf{x}_N + \mathbf{d}_N), \tag{6}$$

and the coordinates of one point in the reference surface, $\mathbf{x}^R(\xi,\eta)$, are computed from $\mathbf{x}_N^R$ using the shape functions of the interface element given in Eq. (4),

$$\mathbf{x}^R(\xi,\eta) = \mathbf{\Phi}^{**}(\xi,\eta)\mathbf{x}_N^R. \tag{7}$$

Once the reference surface is known, the local coordinate system in the current configuration (Fig. 2) is defined by three perpendicular vectors, with unit modulus, expressed by

$$\hat{\mathbf{n}} = \frac{1}{\left\| \frac{\partial \mathbf{x}^R}{\partial \xi} \times \frac{\partial \mathbf{x}^R}{\partial \eta} \right\|} \left(\frac{\partial \mathbf{x}^R}{\partial \xi} \times \frac{\partial \mathbf{x}^R}{\partial \eta} \right), \qquad \hat{\mathbf{t}}_1 = \frac{1}{\left\| \frac{\partial \mathbf{x}^R}{\partial \xi} \right\|} \frac{\partial \mathbf{x}^R}{\partial \xi}, \qquad \hat{\mathbf{t}}_2 = \hat{\mathbf{n}} \times \hat{\mathbf{t}}_1, \tag{8}$$

where $\hat{\mathbf{n}}$ is normal to the surface and $\hat{\mathbf{t}}_1$ and $\hat{\mathbf{t}}_2$ are tangential to the surface. The 3×3 rotation matrix from the global coordinate system to the current local one, $\mathbf{R}$, is thus given by

$$\mathbf{R} = \begin{pmatrix} \hat{\mathbf{n}}^{\mathrm{T}} \\ \hat{\mathbf{t}}_1^{\mathrm{T}} \\ \hat{\mathbf{t}}_2^{\mathrm{T}} \end{pmatrix}. \tag{9}$$

Once the local coordinate system is defined in terms of the global one, it is possible to compute the nodal force vector and the tangent stiffness matrix of the interface element. For a large displacement formulation, neglecting inertia and body forces, the virtual work expression for a body of volume V containing various cohesive surfaces denoted by S_{coh} can be written in the form

$$\int_V \boldsymbol{\sigma}\nabla^s \delta\mathbf{u}\,\mathrm{d}V + \int_{S_{\mathrm{coh}}} \delta\Delta\mathbf{u}^{\mathrm{T}}\mathbf{t}_{\mathrm{coh}}\,\mathrm{d}S_{\mathrm{coh}} = \int_{S_{\mathrm{ext}}} \delta\mathbf{u}^{\mathrm{T}}\mathbf{t}_{\mathrm{ext}}\,\mathrm{d}S_{\mathrm{ext}}, \tag{10}$$

where $\boldsymbol{\sigma}$ is the Cauchy stress tensor, $\mathbf{u}$ the displacement field, $\Delta\mathbf{u}$ the relative displacement between point pairs on opposing sides of the cohesive surface (which had the same position in the initial configuration), and $\mathbf{t}_{\mathrm{coh}}$ and $\mathbf{t}_{\mathrm{ext}}$ stand for the tractions acting, respectively, across the cohesive surfaces and on the external surfaces in the current configuration.

The nodal forces in the interface element are given by a 36×1 vector, $\mathbf{f}_N^{\mathrm{el}}$, computed as

$$\mathbf{f}_N^{\mathrm{el}} = \int_0^1 \int_0^1 \mathbf{\Phi}^{\mathrm{T}}\mathbf{R}^{\mathrm{T}}\mathbf{t}_{\mathrm{loc}} J\,\mathrm{d}\xi\,\mathrm{d}\eta = \sum_j \omega_j \mathbf{\Phi}^{\mathrm{T}}\mathbf{R}^{\mathrm{T}}\mathbf{t}_{\mathrm{loc}} J, \tag{11}$$

where $\mathbf{t}_{\mathrm{loc}}$ is the 3×1 vector which provides the 3 components (one normal and two tangential) of the tractions acting on the cohesive surface in the current configuration as a function of the relative displacement between the element surfaces in local coordinates. J is the Jacobian of the transformation

between the natural coordinates (ξ,η) and Cartesian coordinates in relation to the reference surface in the current configuration expressed as

$$J=\sqrt{\left(\frac{D(x,y)}{D(\xi,\eta)}\right)^2+\left(\frac{D(x,z)}{D(\xi,\eta)}\right)^2+\left(\frac{D(y,z)}{D(\xi,\eta)}\right)^2}, \tag{12}$$

and ω_j is the weight at the Gauss point j to compute the integrals with the Gauss method. 3-, 7- and 13-point Gauss rules were implemented in the standard interface element and it was found that the 3-point rule provided a good approximation. The 4-point rule (one Gauss point at each linear triangle) was used in the modified interface element.

The 36×36 tangent stiffness matrix for the element, $\mathbf{K}^{\mathrm{el}}$, can be defined as

$$\mathbf{K}^{\mathrm{el}}=\frac{\partial\mathbf{f}_N^{\mathrm{el}}}{\partial\mathbf{d}^{\mathrm{el}}}=\int_{\mathrm{el}}\mathbf{\Phi}^{\mathrm{T}}\frac{\partial\mathbf{t}}{\partial\Delta\mathbf{u}}\mathbf{\Phi}\,\mathrm{d}S_{\mathrm{el}}, \tag{13}$$

and this leads to

$$\mathbf{K}^{\mathrm{el}}=\int_0^1\int_0^1\mathbf{\Phi}^{\mathrm{T}}\mathbf{R}^{\mathrm{T}}\mathbf{C}_{\mathrm{loc}}\mathbf{R}\mathbf{\Phi}J\,\mathrm{d}\xi\,\mathrm{d}\eta=\sum_j\omega_j\mathbf{\Phi}^{\mathrm{T}}\mathbf{R}^{\mathrm{T}}\mathbf{C}_{\mathrm{loc}}\mathbf{R}\mathbf{\Phi}J, \tag{14}$$

where $\mathbf{C}_{\mathrm{loc}}$ is a 3×3 matrix defined as

$$\mathbf{C}_{\mathrm{loc}}=\frac{\partial\mathbf{t}_{\mathrm{loc}}}{\partial\Delta\mathbf{u}_{\mathrm{loc}}}, \tag{15}$$

and $\Delta\mathbf{u}_{\mathrm{loc}}=\mathbf{R}\Delta\mathbf{u}$ stands for the relative displacement between the interface element surfaces in the current local coordinate system.

2.2. Constitutive equation for the cohesive crack

The interface element formulated above can accommodate any cohesive crack model which relates the stresses transferred across the crack with the relative displacement between the crack surfaces. They are introduced in the element formulation through the vector $\mathbf{t}_{\mathrm{loc}}$ and the matrix $\mathbf{C}_{\mathrm{loc}}$. In order to validate the new interface element, the cohesive law used by Needleman (1987) to study decohesion between a rigid sphere and an elasto-plastic matrix was implemented here. The normal and tangential components of the interface tractions are derived from an elastic potential, ϕ, which depends only on the normal (Δu_{n}) and tangential (Δu_{t1} and Δu_{t2}) relative displacements between the crack surfaces according to

$$\begin{aligned}\phi(\Delta u_{\mathrm{n}},\Delta u_{\mathrm{t1}},\Delta u_{\mathrm{t2}})=\frac{27t_{\mathrm{c}}\Delta u_{\mathrm{c}}}{4}\Bigg\{&\frac{1}{2}\left(\frac{\Delta u_{\mathrm{n}}}{\Delta u_{\mathrm{c}}}\right)^2\left[1-\frac{4}{3}\frac{\Delta u_{\mathrm{n}}}{\Delta u_{\mathrm{c}}}+\frac{1}{2}\left(\frac{\Delta u_{\mathrm{n}}}{\Delta u_{\mathrm{c}}}\right)^2\right]+\frac{\gamma}{2}\left(\frac{\Delta u_{\mathrm{t1}}}{\Delta u_{\mathrm{c}}}\right)^2\left[1-2\frac{\Delta u_{\mathrm{n}}}{\Delta u_{\mathrm{c}}}+\left(\frac{\Delta u_{\mathrm{n}}}{\Delta u_{\mathrm{c}}}\right)^2\right]\\&+\frac{\gamma}{2}\left(\frac{\Delta u_{\mathrm{t2}}}{\Delta u_{\mathrm{c}}}\right)^2\left[1-2\frac{\Delta u_{\mathrm{n}}}{\Delta u_{\mathrm{c}}}+\left(\frac{\Delta u_{\mathrm{n}}}{\Delta u_{\mathrm{c}}}\right)^2\right]\Bigg\}\end{aligned} \tag{16}$$

for $\Delta u_{\mathrm{n}}<\Delta u_{\mathrm{c}}$, where t_{c} is the maximum normal stress carried by the interface undergoing a purely normal separation ($\Delta u_{\mathrm{t1}}=\Delta u_{\mathrm{t2}}=0$) and Δu_{c} is the relative normal displacement between the crack faces at which all the cohesive forces vanish. The parameter γ specifies the ratio of normal to shear stiffness of the interface with $\gamma=0$, indicating that the cohesive element only transfers normal stresses. Evidently, the normal (t_{n}) and tangential (t_{t1} and t_{t2}) tractions at the interface can be computed by derivating the elastic potential with respect to the corresponding relative displacements between the crack faces, and the $\mathbf{t}_{\mathrm{loc}}$ vector is given by

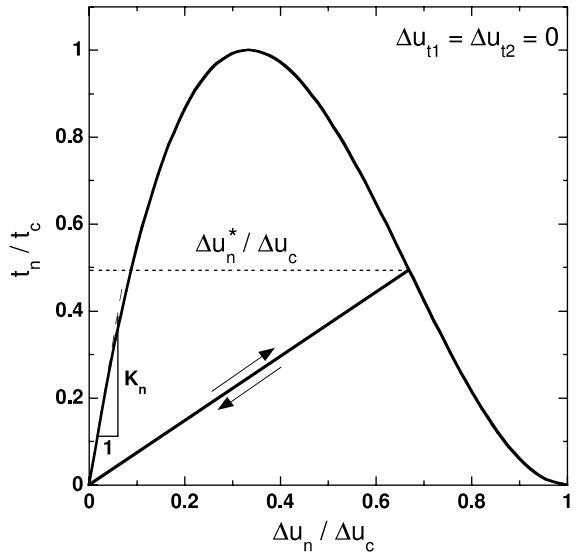

Fig. 3. Normal traction transferred through the cohesive crack as a function of the normal opening between the crack faces when $\Delta u_{t1} = \Delta u_{t2} = 0$.

$$\mathbf{t}_{loc} = \begin{pmatrix} t_n(\Delta u_n, \Delta u_{t1}, \Delta u_{t2}) \\ t_{t1}(\Delta u_n, \Delta u_{t1}) \\ t_{t2}(\Delta u_n, \Delta u_{t2}) \end{pmatrix} = \begin{pmatrix} -\frac{\partial \phi}{\partial \Delta u_n} \\ -\frac{\partial \phi}{\partial \Delta u_{t1}} \\ -\frac{\partial \phi}{\partial \Delta u_{t2}} \end{pmatrix} \quad \text{if } \Delta u_n \leqslant \Delta u_c, \tag{17}$$

and $t_n = t_{t1} = t_{t2} = 0$ if $\Delta u_n > \Delta u_c$. The $\mathbf{C}_{loc}$ matrix is immediately obtained from $\mathbf{t}_{loc}$ following Eq. (15).

The normal tractions transferred across the cohesive crack when $\Delta u_{t1} = \Delta u_{t2} = 0$ are plotted in Fig. 3 as a function of the normal opening between the crack faces. This figure also shows the three main parameters which control the cohesive crack behavior, namely the maximum normal traction, t_c, the critical normal opening at which all tractions disappear, Δu_c, and the fracture energy of the interface, which is given by the area under the t_n–Δu_n curve in the Figure, and which can also be obtained as $\phi(\Delta u_c)$. Evidently, the fracture energy is independent of the fracture path because the stresses are derived from an elastic potential ϕ. These three parameters are related by

$$\phi(\Delta u_c) = \tfrac{9}{16} t_c \Delta u_c. \tag{18}$$

It should be noted that the initial slope of the t_n–Δu_n curve is not infinity, and thus the interface element introduces a certain initial flexibility between the solid continuum elements in the finite element mesh which should not exist because its initial thickness is zero. Evidently, this may lead to an overly flexible response—and to an incorrect stress distribution—if the initial stiffness is too low. On the contrary, a poorly conditioned set of equations may arise if the initial stiffness is too large. In many cohesive crack models, the initial stiffness is a free parameter, whose minimum value is selected by the user so that the stress distribution before any damage occurs is not perturbed by the presence of the interface elements. However, the initial normal stiffness of the interface in Needleman's model, K_n is a function of the t_c and Δu_c expressed by

$$K_n = \left. \frac{\partial t_n}{\partial \Delta u_n} \right|_{\Delta u_n \to 0} = \frac{27}{4} \frac{t_c}{\Delta u_c}, \tag{19}$$

and it should be checked that this value is large enough.

The constitutive equation for the cohesive crack given by Eq. (17) is elastic and the stresses transferred through the crack obey the same law when the crack opens or closes. This behavior, which neglects the damage introduced at the interface by the partial opening, is relevant when the normal opening decreases upon loading due to changes in the external loading path or to an internal stress redistribution induced, for instance, by the sudden failure of neighbor reinforcements. It was included in our analysis through a damage parameter $\Delta u_{\mathrm{n}}^{*}$, which stands for the maximum value of Δu_{n} attained at a given loading step during the analysis. If the new value of Δu_{n} in the next loading step surpasses $\Delta u_{\mathrm{n}}^{*}$, the tractions at the cohesive crack are governed by Eq. (17), and $\Delta u_{\mathrm{n}}^{*}$ is updated. Otherwise, the stresses transferred through the cohesive crack are given by

$$\mathbf{t}_{\mathrm{loc}} = \begin{pmatrix} t_{\mathrm{n}} \\ t_{\mathrm{t1}} \\ t_{\mathrm{t2}} \end{pmatrix} = \begin{pmatrix} -\frac{\partial \phi}{\partial \Delta u_{\mathrm{n}}}(\Delta u_{\mathrm{n}}^{*}, \Delta u_{\mathrm{t1}}, \Delta u_{\mathrm{t2}}) \left(\frac{\Delta u_{\mathrm{n}}}{\Delta u_{\mathrm{n}}^{*}} \right) \\ -\frac{\partial \phi}{\partial \Delta u_{\mathrm{t1}}}(\Delta u_{\mathrm{n}}^{*}, \Delta u_{\mathrm{t1}}) \\ -\frac{\partial \phi}{\partial \Delta u_{\mathrm{t2}}}(\Delta u_{\mathrm{n}}^{*}, \Delta u_{\mathrm{t2}}) \end{pmatrix} \quad \text{if } \Delta u_{\mathrm{n}} \leqslant \Delta u_{\mathrm{n}}^{*}, \tag{20}$$

where the relationship between the normal tractions and the normal opening between the crack faces is linear, as shown in Fig. 3. The corresponding $\mathbf{C}_{\mathrm{loc}}$ matrix is obtained from $\mathbf{t}_{\mathrm{loc}}$ following Eq. (15).

3. Global solution technique

The interface element described above was implemented in the finite element code Abaqus (2002) using the user subroutine UEL, which computes the nodal forces vector (Eq. (11)) and the element tangent stiffness matrix (Eq. (13)) at each load increment in each interface element. They are assembled with the rest of the internal force vectors and stiffness matrices to obtain the global stiffness matrix of the structure. The analyses presented in the following sections were performed with this code within the context of the finite deformations theory and quasi-static deformations with body forces neglected. The nucleation and growth of damage by progressive fracture of the interface elements led sometimes to the occurrence of snap-back in the load–displacement curve of the model, e.g. the simultaneous reduction of the load and of the displacement at the load point. Neither load-controlled nor displacement-controlled boundary conditions can be used with the standard non-linear Newton–Raphson scheme to obtain the whole load–displacement curve of the model under such conditions, and sophisticated control algorithms are normally used. The modified Riks method (Crisfield, 1986) is available in Abaqus to deal with this kind of problems, but it does not always converge, particularly if the curvature of the load–displacement curve is very high.

Another control strategy relays in finding a variable that increases monotonically during the whole loading history. For instance, the crack opening displacement is a good choice if there is only one crack in the structure but the random apparition of interface and/or particle cracks throughout the model may lead to the closing of one crack during deformation as a result of local relaxations caused by the redistribution of stresses. However, the sum of the relative openings of all the interface elements in the model along the main loading direction always increases during loading and can be used to control the problem as shown below.

Let N_1 and N_2 be two paired nodes on opposite surfaces of an interface element. Assuming that the global load is applied along the x axis, the relative displacement between the paired nodes in this direction can be related linearly to the force in a new dummy node N_{c} by $P_x^{N_{\mathrm{c}}} = d_x^{N_1} - d_x^{N_2}$. A dummy element made up by nodes N_1, N_2 and N_{c} is created, and the corresponding stiffness matrix is given by

$$\begin{pmatrix} 0 & 0 & 0 \\ 0 & 0 & 0 \\ 1 & -1 & 0 \end{pmatrix} \begin{pmatrix} d_x^{N_1} \\ d_x^{N_2} \\ d_x^{N_{\mathrm{c}}} \end{pmatrix} = \begin{pmatrix} P_x^{N_1} \\ P_x^{N_2} \\ P_x^{N_{\mathrm{c}}} \end{pmatrix}. \tag{21}$$

Similarly, if N_L is the node were the loads are applied, the load in this node, $P_x(N_L)$, is made equal to the displacement of the dummy node along the x axis $d_x^{N_c}$, and this relation is introduced through the stiffness matrix of another element as

$$\begin{pmatrix} 0 & 1 \\ 0 & 0 \end{pmatrix} \begin{pmatrix} d_x^{N_L} \\ d_x^{N_c} \end{pmatrix} = \begin{pmatrix} P_x^{N_L} \\ P_x^{N_c} \end{pmatrix}. \tag{22}$$

The element matrix of Eq. (21) is defined in all the paired nodes at the interface elements, and the corresponding stiffness matrices, together with the stiffness matrix of Eq. (22), are assembled with the rest of the elements in the model. The analysis proceeds by applying a *force* to the node N_c, which is the sum of all the relative displacements between the paired nodes at the interface elements along the x direction. The displacement on node N_c in this direction is precisely the external load applied on node N_L to obtain equilibrium. As it will be shown below, this control strategy was able to capture the whole load–displacement curve in problems with showed marked snap-backs due to sudden fracture of brittle spheres within the microstructure. Otherwise, this control strategy increases the computing time because the global stiffness matrix is not symmetric.

4. Element validation

The interface element was validated using as benchmark the numerical results of Needleman (1987), who analyzed the interface decohesion of a rigid sphere embedded in a cylinder of an elasto-plastic matrix. The original simulation was carried out within the context of an axisymmetric unit cell with symmetric boundary conditions (Fig. 4a). The sphere radius, r_0, was equal to $0.25R$, and the volume fraction occupied by the rigid sphere in the cylindrical cell was 1.04%. The equivalent three-dimensional model was made up of a 30° portion of the upper half of the solid cylinder under consideration (Fig. 4b). Symmetric boundary

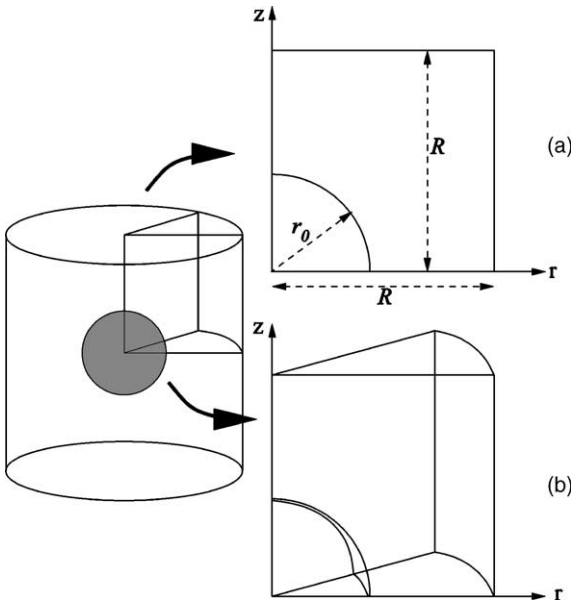

Fig. 4. Spherical particle embedded in a cylindrical cell. (a) 2D axisymmetric model used in Needleman (1987). (b) Equivalent 3D model.

conditions were imposed on the cylinder external and lateral surfaces, and the model was meshed with modified 10-node tetrahedra. The mesh size was similar to that reported in Needleman (1987). The cylindrical cells were loaded by applying uniform displacements on the cylinder upper surface along the z axis ($u_z = v$ on $z = R$) and on the external surface along the r axis ($u_r = u$ on $r = R$). Both displacements were related during the analysis by

$$\frac{F_r}{2F_z}\frac{(1+u/R)}{(1+v/R)} = \frac{\sigma_r}{\sigma_z} = \frac{1}{2}, \tag{23}$$

where F_r and F_z stand for the total forces applied, respectively, on the external and upper cylinder surfaces, and σ_r and σ_z are the corresponding components of the Cauchy stress acting on these surfaces. These boundary conditions were introduced in Abaqus through a user subroutine to impose the non-linear multi-point constraints.

In the original analysis by (Needleman, 1987), the matrix was modeled as an elastic-viscoplastic isotropically hardening solid. However, as the influence of the strain rate on the flow stress was very weak, it was neglected in our simulations, and the matrix was considered an elasto-plastic solid with isotropic hardening following the incremental theory of plasticity and the Von Mises yield criterion. The matrix elastic constants were $E = 200$ GPa and $v = 0.30$, and the flow stress, $\bar{\sigma}$, was expressed as a function of accumulated plastic strain, $\bar{\epsilon}$ as,

$$\bar{\sigma} = \sigma_0\left(1 + \frac{E}{\sigma_0}\bar{\epsilon}\right)^{0.1}, \tag{24}$$

with $\sigma_0 = 400$ MPa. The sphere–matrix interface was modeled with the corresponding modified interface elements presented above with four integration points, one at the center of each linear triangle. The constitutive equation for the cohesive crack followed Eq. (17), and the interface properties were given by $t_c = 3\sigma_0$, $\gamma = 10$, and $\Delta u_c = 0.01 r_0$.

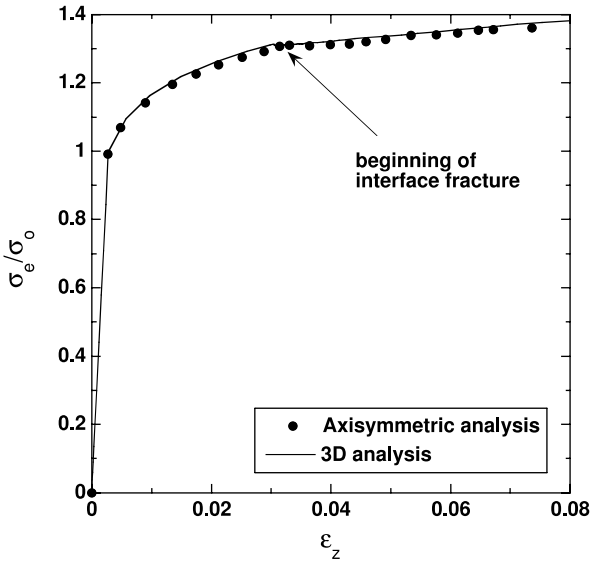

Fig. 5. Evolution of the effective stress in the cylindrical cell, σ_e, as a function of the applied strain in the sphere decohesion problem. The results obtained with the 2D axysimmetric and the three-dimensional models are practically superposed.

The evolution of the effective stress on the cylindrical cell, $\sigma_e = |\sigma_z - \sigma_r|$, as a function of the logarithmic strain along the z axis, $\epsilon_z = \ln(1 + v/R)$, is plotted in Fig. 5 for the 2D axisymmetric and the 3D models. Both curves are practically superposed, validating the new interface element, and it is particularly worth noting that the onset of interface fracture (marked with an arrow in the figure) coincided in both simulations. The contour plots in Fig. 6 show the effect of interfacial fracture on the pattern of the accumulated

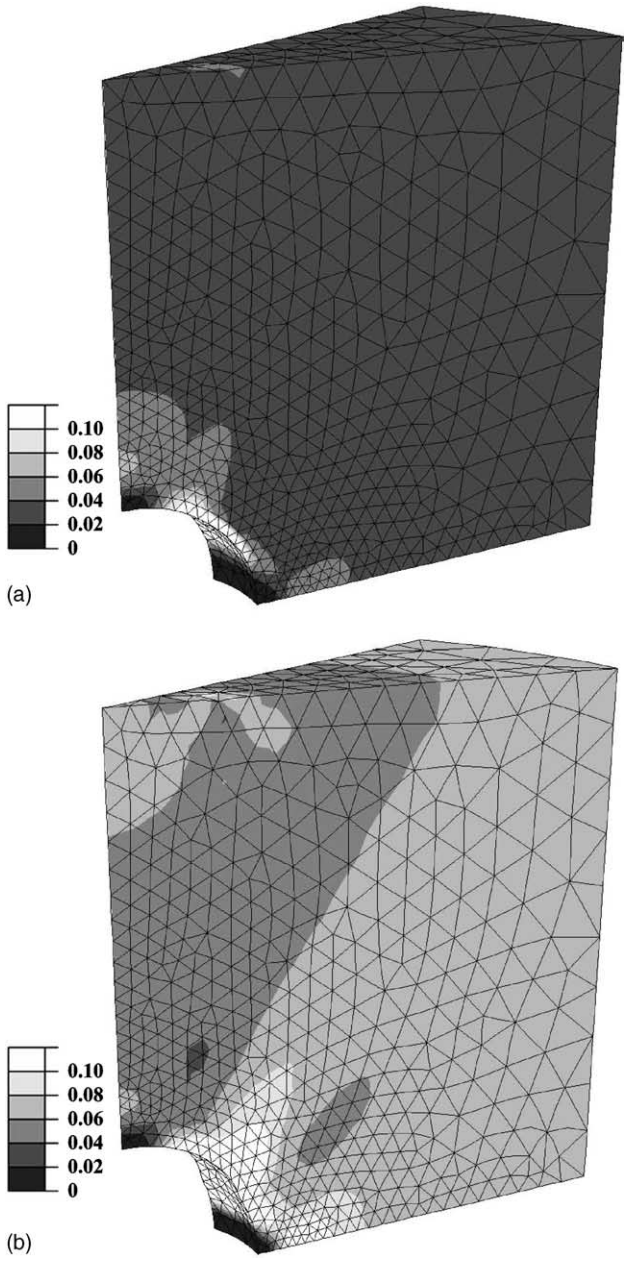

Fig. 6. Contour plots of the accumulated plastic strain in the matrix: (a) $\epsilon_z = 3.5\%$ and (b) $\epsilon_z = 8.8\%$.

plastic strain in the matrix. Before decohesion, the maximum plastic strains were concentrated in a very thin layer surrounding the rigid sphere (Fig. 6a). They spread very quickly throughout the cylindrical cell once the interface was broken and the matrix deformation was no longer constrained by the rigid particle.

5. Control algorithm validation

The ability of the new control algorithm to obtain the whole load–displacement curve of the model was demonstrated by simulating the tensile deformation of a sphere-reinforced composite including particle fracture. The composite behavior was determined by the finite element analysis of a periodic cubic cell of volume L^3 containing a random and homogeneous dispersion of 7 non-overlapping identical spheres. The volume fraction of spheres within the composite was 15% and the sphere radius, r_0 was computed from the unit cell volume and the number of spheres. Sphere center positions were generated randomly and sequentially, and the ith particle was accepted if the distance between its center and all the previous particles exceeds a minimum value, $2.07r_0$, imposed by the practical limitations of creating an adequate finite element mesh. If the surface of the ith particle cut any of the cubic unit cell surfaces, this condition was checked with the particles near the opposite surface because of the periodic microstructure of the composite. In addition, the particle surface should not be very close to the cubic unit cell faces to prevent the presence of distorted finite elements during meshing.

Finite element discretizations of a cubic unit cell were created from the particle center distributions. Spheres were generated from the particle centers and radius, and those intersecting the cube faces were split into an appropriate number of parts and copied to the opposite sides of the cube. Three faces of the cube were meshed with quadratic triangles, and the meshes were copied to the opposite sides (Fig. 7). The pairing of the nodes in opposite cube faces was necessary to apply the periodic boundary conditions. The model

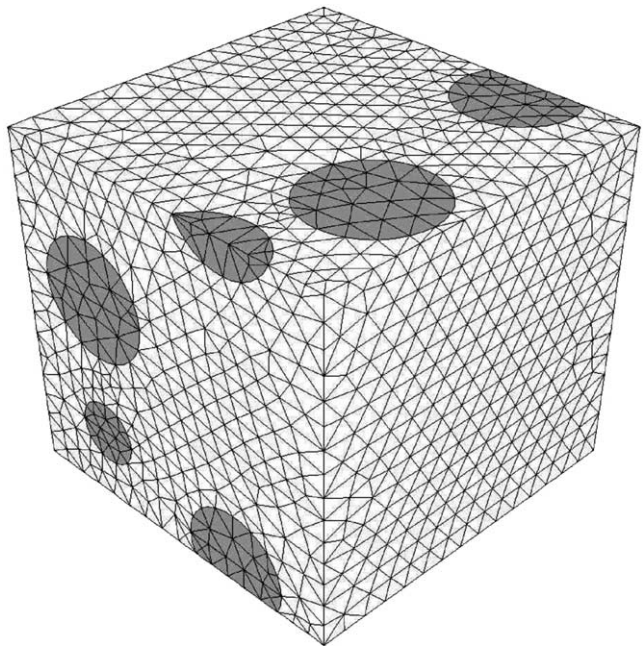

Fig. 7. Finite element discretization of three concurrent faces of the cubic unit cell. The spherical particles are shaded. The three other surfaces have the same discretization because the microstructure is periodic.

volume (matrix and spheres) was meshed using the modified 10-node tetrahedra available in Abaqus (2002) and more details about the unit cell generation and the finite element discretization can be found in Segurado and LLorca (2002) and Segurado et al. (2003). According to the experimental evidence (Fig. 1b), it was assumed that particle fracture occurred through the equator and a plane of modified interface elements was introduced at the equator of each spherical particle perpendicularly to the main loading axis.

If three concurrent edges of the cube stand for the axes of coordinates xyz, the periodic boundary conditions can be expressed as a function of the displacement vector $\mathbf{u}$ as

$$\begin{aligned} \mathbf{u}(x,y,0) - \mathbf{u}_z &= \mathbf{u}(x,y,L), \\ \mathbf{u}(x,0,z) - \mathbf{u}_y &= \mathbf{u}(x,L,z), \\ \mathbf{u}(0,y,z) - \mathbf{u}_x &= \mathbf{u}(L,y,z). \end{aligned} \tag{25}$$

Tensile loading along the z axis is obtained with $\mathbf{u}_z = (0,0,w)$, $\mathbf{u}_x = (u,0,0)$, and $\mathbf{u}_y = (0,v,0)$, where $\epsilon_z = \ln(1+w/L)$ is the applied logarithmic strain along the z axis and u and v are computed from the conditions

$$\int_\Omega t_x \,\mathrm{d}\Omega = 0 \ \text{ on } x = L \quad \text{and} \quad \int_\Omega t_y \,\mathrm{d}\Omega = 0 \ \text{ on } y = L, \tag{26}$$

where t_x and t_y stand for the normal tractions acting on the current cell faces contained, respectively, in the planes $x = L$ and $y = L$.

The spherical reinforcements behaved as elastic and isotropic solids with $E_s = 400$ GPa and $\nu_s = 0.2$. The matrix was modeled as an isotropic elasto-plastic solid with isotropic hardening following the incremental theory of plasticity and the Von Mises yield criterion. The matrix elastic constants were $E_m = 70$ GPa and $\nu_m = 0.33$, and the flow stress, $\bar{\sigma}$, was expressed as a function of accumulated plastic strain, $\bar{\epsilon}$, as,

$$\bar{\sigma} = 400\bar{\epsilon}^{0.15}. \tag{27}$$

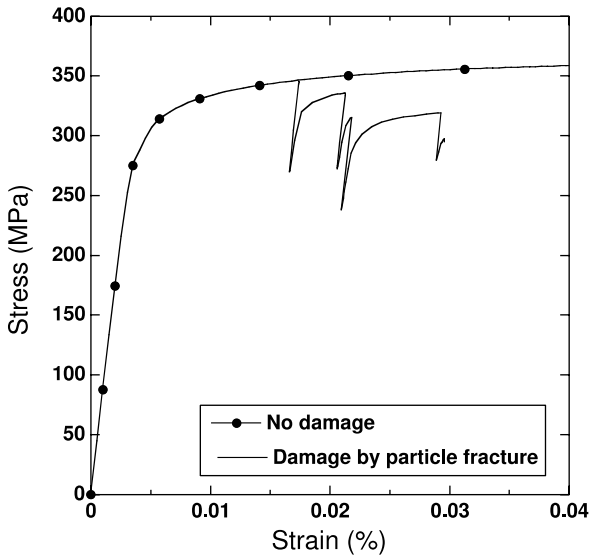

Fig. 8. Simulations of the tensile deformation of an elasto-plastic matrix reinforced with a 15 vol.% of brittle ceramic spheres with and without particle fracture.

These values are typical of an aluminum alloy reinforced with stiff ceramic particles (alumina or silicon carbide). The cohesive model introduced in Section 2.2 was used in the interface elements to simulate sphere fracture with $t_c = 500$ MPa and $\Delta u_c = 0.1$ μm ($= 0.01 r_0$), which led to a fracture energy of 28 J/m^2, and $\gamma = 1$.

The results of the simulation of the composite tensile stress–strain curve with and without reinforcement fracture are plotted in Fig. 8. They are superposed up to an applied strain of ≈1.7%, when the first sphere was broken. Reinforcement fracture occurred suddenly because the spheres were brittle, with very low

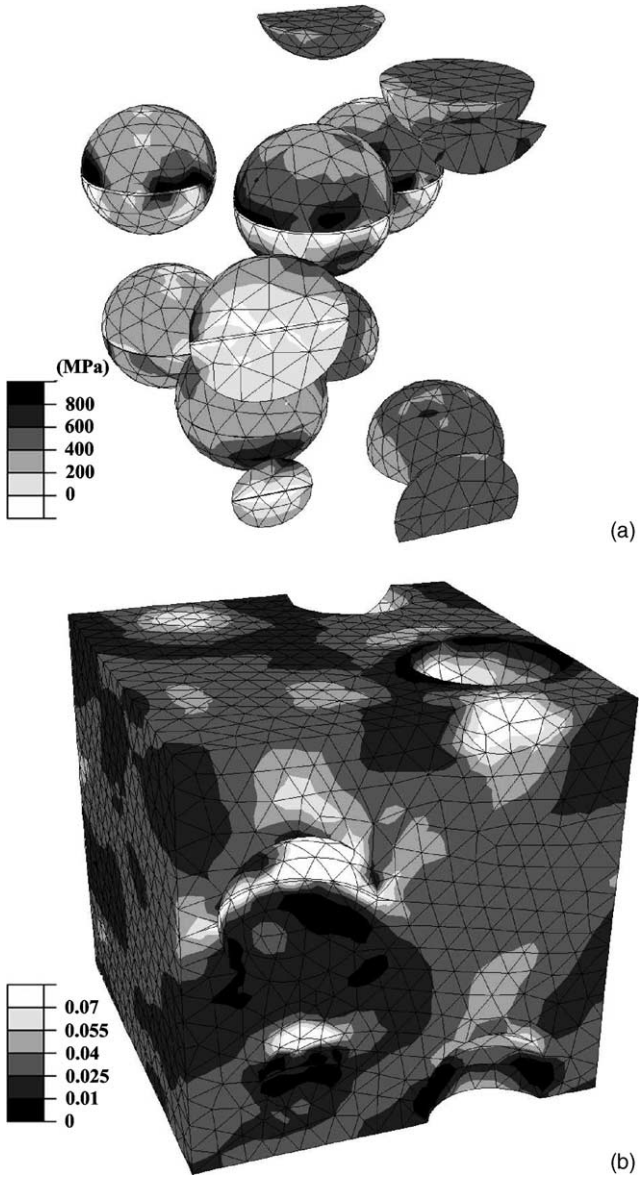

Fig. 9. (a) Contour plot of σ_z in the spheres. (b) Contour plot of the accumulated plastic strain in the matrix. The loading direction (z) is vertical, and the applied strain was xx%. The displacements along the z axis were increased by a factor of four to show the cracks in the broken spheres.

fracture energy, and this led to a marked reduction in the average composite stress and strain. The pronounced snap-back was perfectly captured by the control algorithm, and the deformation continued until a new sphere was fractured, leading to another snap-back. The sawtooth shape of the stress–strain curve shows that the spheres were fractured progressively during deformation even though they have the same strength because they did not carry the same load. Of course, the number of spheres in the cubic unit cell was too low to capture adequately the average composite behavior, but this was not the focus of the simulation, which was aimed at checking the new control algorithm.

The contour plots of σ_z in the spheres and of the accumulated plastic strain in the matrix are shown in Fig. 9a and b, respectively, at the end of the analysis. The stresses in the z direction are close to zero at the center of the broken spheres, but not at the surface due to the load transfer from the matrix. This figure also shows that three of the sphere cracks were approximately coplanar, indicating that particle fracture was localized at a given plane within the composite. The load shed by the first broken particle was partially taken up by neighbor particles in the same plane, which failed shortly afterwards. Moreover, the sphere cracks opened up as the applied strain increased, and the plastic strain in the matrix was particularly intense near the broken spheres, as is shown in the contour plot of the accumulated plastic strain in the matrix (Fig. 9b). This will lead sooner or later to the ductile matrix failure, and to the final composite fracture. The numerical simulation of matrix failure was not considered here but it was addressed in another investigation (LLorca and Segurado, 2004).

6. Conclusions

Recent developments in computational micromechanics were aimed at simulating the overall properties of particle-reinforced composites by the numerical simulation in three-dimensions of a representative volume element which mimics accurately the actual microstructure. However, it is well known that the mechanical behavior of these composites is often controlled by the nucleation of damage in the form of particle fracture and matrix/particle decohesion, and a new three-dimensional quadratic interface finite element was developed to include these effects in the simulations. The element was made up of two 6-noded triangular surfaces which initially lie together and connect the faces of adjacent quadratic tetrahedra, the only elements supported by the automatic meshing algorithms used in the discretization of the complex composite microstructure. Two versions of the element were developed; the *standard* element was compatible with standard, isoparametric 10-node tetrahedra, while the *modified* interface element was compatible with the composite tetrahedra of Thoutireddy et al. (2002) and with the modified 10-node tetrahedra of Abaqus (2002).

The element was developed within the framework of implicit analysis and large displacements. The relative displacement of the element faces generates normal and shear stresses depending on the constitutive equation of the cohesive crack, which is independent of the element formulation. The new interface element was programmed as a user subroutine in Abaqus (2002) and was validated by comparison with the numerical results of Needleman (1987), who analyzed the interface decohesion of a rigid sphere embedded in an elasto-plastic matrix.

The application of the new interface element to simulate damage (by particle fracture or interface decohesion) in cells containing a large number of particles introduced a new problem. The progressive fracture of the interface elements led sometimes to the occurrence of snap-back in the load–displacement curve of the model, e.g. the simultaneous reduction of the load and of the displacement at the load point. As the standard control algorithms were not able to provide an unconditional convergence, a new control strategy was developed. The new technique relays in finding a variable that increases monotonically during the whole loading history, and this variable was the sum of the relative openings of all the interface elements in the model along the main loading direction. The new control technique was also implemented in Abaqus (2002) as another user subroutine, and it was successfully validated in the numerical simulation of the

tensile deformation of a sphere-reinforced composite which presented severe snap-backs in the load–displacement curve due to the progressive fracture of the spheres.

Appendix A. Shape functions

The shape functions of the interface element connecting two 10-node tetrahedra faces (6-node triangles) have to match the shape functions of the tetrahedra at that face. Thus, the shape functions of the standard interface element, compatible with those of the standard quadratic 10-node tetrahedra, are expressed as

$$\begin{aligned}
\phi_1(\xi,\eta) &= 2\left(\tfrac{1}{2}-\xi-\eta\right)(1-\xi-\eta),\\
\phi_2(\xi,\eta) &= 2\xi\left(\xi-\tfrac{1}{2}\right),\\
\phi_3(\xi,\eta) &= 2\eta\left(\eta-\tfrac{1}{2}\right),\\
\phi_4(\xi,\eta) &= 4\xi(1-\xi-\eta),\\
\phi_5(\xi,\eta) &= 4\xi\eta,\\
\phi_6(\xi,\eta) &= 4\eta(1-\xi-\eta),
\end{aligned} \tag{A.1}$$

where the position of the nodes on the triangular surface is shown in Fig. 10.

In the case of the modified interface element, the quadratic triangle is subdivided into four linear triangles, as shown on Fig. 10. The shape functions at (ξ,η) depend on the particular subtriangle in which the point is located, and they are expressed by (Thoutireddy et al., 2002),

Triangle I

$$\begin{aligned}
\phi_1(\xi,\eta) &= 1-2\xi-2\eta,\\
\phi_4(\xi,\eta) &= 2\xi,\\
\phi_6(\xi,\eta) &= 2\eta.
\end{aligned} \tag{A.2}$$

Triangle II

$$\begin{aligned}
\phi_2(\xi,\eta) &= 2\left(\xi-\tfrac{1}{2}\right),\\
\phi_4(\xi,\eta) &= 1-2\left(\xi-\tfrac{1}{2}\right)-2\eta,\\
\phi_5(\xi,\eta) &= 2\eta.
\end{aligned} \tag{A.3}$$

Triangle III

$$\begin{aligned}
\phi_3(\xi,\eta) &= 2\left(\eta-\tfrac{1}{2}\right),\\
\phi_5(\xi,\eta) &= 2\xi,\\
\phi_6(\xi,\eta) &= 1-2\xi-2\left(\eta-\tfrac{1}{2}\right).
\end{aligned} \tag{A.4}$$

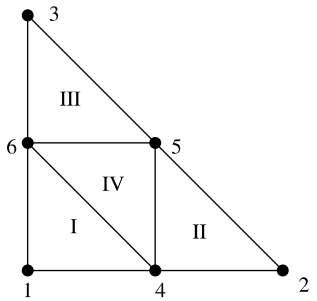

Fig. 10. Node positions and triangle subdivisions for the shape functions of the modified interface element.

Triangle IV

$$\begin{aligned}\phi_4(\xi,\eta) &= 2\left(\tfrac{1}{2}-\eta\right),\\ \phi_5(\xi,\eta) &= 2\xi+2\eta-1,\\ \phi_6(\xi,\eta) &= 2\left(\tfrac{1}{2}-\xi\right).\end{aligned} \tag{A.5}$$

References

Abaqus, 2002. Users' Manual. Hibbitt, Karlsson, and Sorensen, Inc.

Babout, L., Maire, E., Buffiere, J.Y., Fougeres, R., 2001. Characterization by X-ray computed tomography of decohesion, porosity growth and coalescence in model metal matrix composites. Acta Materialia 49, 2055–2063.

Cantwell, W.J., Roulin-Moloney, A.C., 1989. Fractography and failure mechanisms of unfilled and particulate filled epoxy resins. In: Fractography and Failure Mechanisms of Unfilled and Particulate Filled Epoxy Resins. Elsevier Applied Science, London, pp. 234–289.

Crisfield, M.A., 1986. Snap-through and snap-back response in concrete structures and the dangers of under-integration. International Journal for Numerical Methods in Engineering 22, 751–767.

de Andrés, A., Pérez, J.L., Ortiz, M., 1999. Elasto-plastic finite element analysis of three-dimensional fatigue crack growth in aluminum shafts subjected to axial loading. International Journal of Solids and Structures 36, 2231–2258.

Eckschlager, A., Han, W., Böhm, H.J., 2002. A unit cell model for brittle fracture of particles embedded in a ductile matrix. Computational Materials Science 25, 85–91.

Ghosh, S., Ling, Y., Majumdar, B., Kim, R., 2000. Interfacial debonding analysis in multiple fiber reinforced composites. Mechanics of Materials 32, 561–591.

González, C., LLorca, J., 1998. Microstructural factors controlling the strength and ductility of particle-reinforced metal-matrix composites. Journal of the Mechanics and Physics of Solids 46, 1–28.

Gusev, A.A., 1997. Representative volume element size for elastic composites: a numerical study. Journal of the Mechanics and Physics of Solids 45, 1449–1459.

Hashagen, F., de Borst, R., 2000. Numerical assessment of delamination in fibre metal laminates. Computational Methods in Applied Mechanical Engineering 185, 141–159.

Kanetake, N., Nomura, M., Choh, T., 1995. Continuous observation of microstructural degradation during tensile loading of particle reinforced aluminium composites. Materials Science and Technology 11, 1246–1252.

LLorca, J., 2000. Void formation in metal matrix composites. In: Comprehensive Composite Materials, vol. 3, Metal-matrix Composites. Pergamon Press, London, pp. 91–115.

LLorca, J., Segurado, J., 2004. Three-dimensional multiparticle cell simulations of deformation and damage in sphere-reinforced composites. Materials Science and Engineering A 365, 267–274.

Lusti, H.R., Hine, P.J., Gusev, A.A., 2002. Direct numerical predictions for the elastic and thermoelastic properties of short fibre composites. Composites Science and Technology 62, 1927–1934.

Michel, J.C., Moulinec, H., Suquet, P., 1999. Effective properties of composite materials with periodic microstructure: a computational approach. Computational Methods in Applied Mechanical Engineering 172, 109–143.

Moloney, A.C., Kausch, H.H., Kaiser, T., Beer, H.R., 1987. Parameters determining the strength and toughness of particulate filled epoxide resins. Journal of Materials Science 22, 381–393.

Needleman, A., 1987. A continuum model for void nucleation by inclusion debonding. Journal of Applied Mechanics 54, 525–531.

Ortiz, M., Pandolfi, A., 1999. Finite deformation irreversible cohesive elements for three-dimensional crack propagation analysis. International Journal for Numerical Methods in Engineering 44, 1267–1282.

Pandolfi, A., Guduru, P., Ortiz, M., Rosakis, A., 2000. Three-dimensional cohesive-element analysis and experiments of dynamic fracture in C300 steel. International Journal of Solids and Structures 37, 3733–3760.

Roychowdhury, S., Roy, D.A., Dodds Jr., R.H., 2003. Ductile tearing in thin aluminium panels; experiments and analyses using large-displacement, 3-D surface cohesive elements. Engineering Fracture Mechanics 69, 983–1002.

Segurado, J., LLorca, J., 2002. A numerical approximation to the elastic properties of sphere-reinforced composites. Journal of the Mechanics and Physics of Solids 50, 2107–2121.

Segurado, J., González, C., LLorca, J., 2003. A numerical investigation of the effect of particle clustering on the mechanical properties of composites. Acta Materialia 51, 2355–2369.

Thoutireddy, P., Molinari, J.F., Repetto, E.A., Ortiz, M., 2002. Tetrahedral composite finite elements. International Journal for Numerical Methods in Engineering 53, 1337–1351.

Tvergaard, V., 1990. Effect of fibre debonding in a whisker-reinforced metal. Materials Science and Engineering A 125, 203–213.

Tvergaard, V., Hutchinson, J.W., 1993. The influence of plasticity on mixed mode interface toughness. Journal of the Mechanics and Physics of Solids 41, 1119–1135.